# Investigation of the fracture of very thin amorphous alumina film during spherical nanoindentation

David Mercier, Vincent Mandrillon, Guillaume Parry, Marc Verdier, Rafael Estevez, Yves Brechet, Tony Maindron

# Investigation of the fracture of very thin amorphous alumina film during spherical nanoindentation

D. Mercier*[1], V. Mandrillon[1], G. Parry[2], M. Verdier[2], R. Estevez[2], Y. Bréchet[2], and T. Maindron[1]

[1]CEA, LETI, MINATEC Campus, F-38054 Grenoble, France
[2]Université de Grenoble, Lab. SIMaP-CNRS, BP 75, St Martin d'Hères, F-38402 Cedex, France

**Abstract**

Thin amorphous alumina layers (10 to 40nm thick) are processed on sputtered aluminum thin film (500nm) by atomic layer deposition (ALD) at low temperature (85°C). Global methodology combining quantitative experimental observations of fracture and numerical modeling is proposed to obtain the fracture strength of ALD thin film on Al layer. First, mechanical properties of the multilayer specimen are characterized by Berkovich nanoindentation, then fracture of ALD alumina is studied through spherical indentation with various tip radius. Spherical indentation load driven-displacement curves display a plateau (pop-in) at a critical load and critical indentation depth. A statistical approach is used to determine pertinent/fracture parameters from pop-in displacement. Careful SEM and AFM observations of indentation imprint exhibit circumferential cracking in agreement with the assumption that the pop-in event is predominantly controlled by the fracture of the oxide layer on the soft Al film. Finally, a numerical model calibrated with experimental results is used in order to predict both the mechanical response prior to the oxide fracture and a value of fracture strength for ALD alumina thin films.

**Abbreviations:** ALD, atomic layer deposition; PVD, physical vapor deposition; TO, thermal oxidation; NI, nanoindentation; MM, membrane model; FE, finite element; FEM, finite element model.

**Keywords:** Thin hard film; ALD alumina; nanoindentation; cracks; pop-in; Weibull statistical analysis; finite element modeling; fracture strength.

## 1 Introduction

Thin amorphous alumina coatings processed by atomic layer deposition (ALD) technique are widely used in the fields of microelectronics, microelectromechanical systems (MEMS), organic light-emitting diodes (OLED), food packaging and biomaterials [1–4]. Such films provides the advantage to be good thermal and electrical insulators, to be hydrophobic, hermetic and biocompatible, and to have good mechanical properties, low stresses and to reduce frictional wear. Thus, ALD coatings are often used as structural layers for MEMS and OLED or as a mechanical protection for soft substrate against wear, shocks and attrition, in an aggressive environment. The understanding of fracture mechanisms and the knowledge of the material property values of thin ALD films is also important for surface engineering and the design of new MEMS and OLED devices.

The fracture of hard thin film on soft substrate has been explored by means of indentation with geometrically self-similar indenters (e.g.: Berkovich, Vickers, conical tip,...) [5–13], or with a spherical indenter [14–18]. The indentation load driven vs displacement curves display a plateau (pop-in) at a critical load and at a critical displacement, which can follow a Weibull type distribution [8, 13]. This plateau is often attributed to the yielding and nucleation of dislocations into the substrate and in some cases to the fracture of the hard film, or to a combination of these two mechanisms evolving in parallel. Moreover, some authors have also studied the fracture of a brittle film on a soft substrate (e.g.: native alumina oxide on aluminum) through electrical contact resistance measurement [19–24], and some of these authors have directly correlated the disruption of such native oxide to the pop-in event [23, 24].

Different approaches have been developed to describe the deformation behaviour of a hard thin film on a soft substrate. Some experimental and numerical works have demonstrated that at yield point the hard film undergoes

*david.mercier@crmgroup.be

a through-thickness fracture arising from a maximum tensile stress around the contact edge, which is an analogous behavior to the cracking of ice on mud, or "crème brûlée" [14, 25–32]. Then, several analytical models, based on a membrane effect, describe the bending and the stretching of the thin film [8, 12, 15, 17, 18, 33, 34]. Finally, energy methods have been used to determine, at first order, the toughness of the film, and then to estimate the amount of energy required to produce cracks in the film [18, 29, 35–37].

The current study focuses on the spherical indentation of thin ALD amorphous alumina layers (10 to 40nm thick), which were processed by atomic layer deposition (ALD) at low temperature, on sputtered aluminum thin films. The first part of this work is devoted to the processing, the microstructural and mechanical characterization of the samples. Then, load driven vs displacement curves made by nanoindentation (NI) were analyzed in order to validate the assumption that the pop-in event is predominantly controlled by the fracture of the oxide film. The observation by scanning electron microscope (SEM) of circumferential cracks in the residual indentation imprints also confirms this hypothesis. A second part of this study deals with the statistical analysis of the fracture events with a Weibull distribution. Then, a numerical model calibrated with experimental results is used in order to predict both the mechanical response prior to the oxide fracture and the radial stress before the pop-in event. Finally, a value of fracture strength for ALD alumina thin film is extracted from finite-element simulations.

## 2 Sample description

Pure aluminum film (540nm thick) was first sputtered by physical vapour deposition (PVD) on a thermally oxidized silicon substrate. 500nm thick $SiO_2$ was obtained by dry thermal oxidation (TO) at a temperature of 1050°C. An average grain size of 410nm and a RMS roughness of 2.7nm were calculated for the aluminum thin film using topography measurement obtained by atomic force microscopy (AFM) (see Figure 1b).

Four alumina layers (10, 20, 30 and 40nm thick) were processed on four identical samples ($Al/SiO_2/Si$) by atomic layer deposition (ALD) at low temperature (85°C), in a Savannah 200 from Cambridge Nanotech, from $Al(CH_3)_3/H_2O$ precursors [4]. The amorphous structure and the thickness of the ALD alumina were controlled by transmission electron microscopy (TEM) (see Figure 1c). A native amorphous 4nm thick aluminum oxide was observed between aluminum thin film and ALD alumina. In a first approximation, the presence of this native alumina was neglected in the extraction of the mechanical properties of materials.

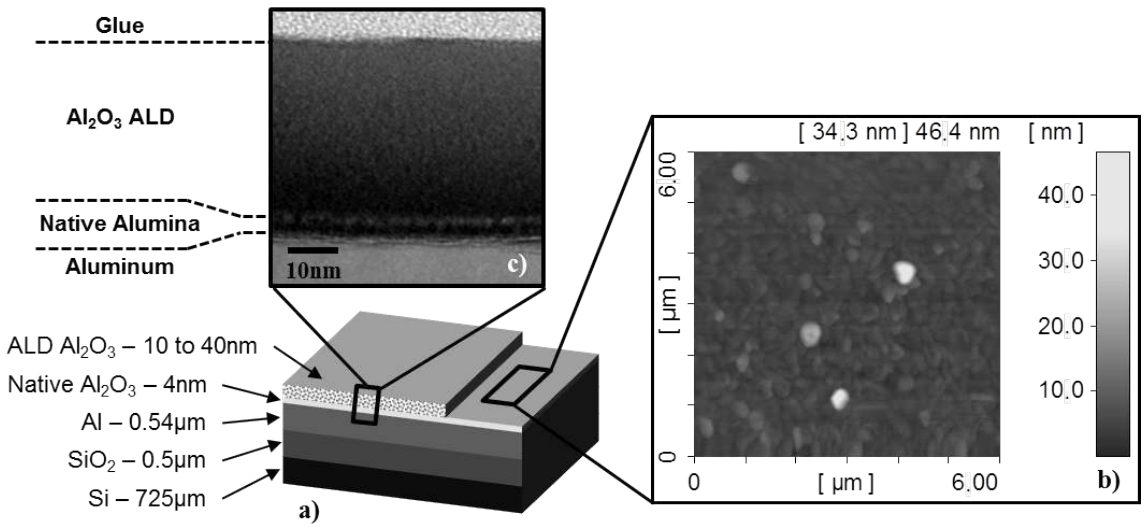


Figure 1: a) Scheme of the multilayer specimen, with b) TEM cross-sectional observation of the 40nm thick ALD alumina coating and c) AFM measurement of the native alumina on the aluminum surface.

The mechanical properties of the underlying aluminum thin film, the $SiO_2$ layer and the silicon substrate were obtained from nanoindentation measurements carried out using a Nanoindenter XP$^{TM}$ (MTS Instruments). 64 measurements were made at room temperature at an acquisition frequency of 10Hz, with a strain rate of $0.05s^{-1}$, for each layer of the specimen, using a Berkovich diamond tip (tip radius of 80nm and tip defect of 5nm), with a continuous

stiffness measurement method (CSM) (at a frequency of 75Hz and an amplitude of 0.5nm). Load ($L$), displacement ($h$) and elastic contact stiffness ($S$) were continuously recorded during indentation. The area function ($A_c$) of the contact depth, was carefully calibrated from measurements done on a fused silica sample, following the procedure given by Oliver and Pharr [38]. Nanoindentation experiments were load-controlled with a total indentation depth of 500nm. Those experiments were not carried out for the four samples with the ALD alumina thin films, given the impossibility to extract valid mechanical properties by means of nanoindentation for such thin coatings, because of the inaccuracy of the calibration of the tip at such small scale, the surface effect (roughness, contamination...) and the effect of underlying layers. Values of Young's modulus and hardness obtained from nanoindentation experiments performed by Bull [39] on a ALD alumina coating deposited at 80°C on a silicon substrate, were used in this work (see Table 1). Reduced Young's moduli ($E'$) were estimated using the well-known Sneddon's relationship Equation (1), with $\beta$ a geometrical correction factor equal to 1.034, in the case of Berkovich indentation. The contact area was calculated for the silicon substrate and the thermal silicon oxide, using the contact depth equation from Oliver and Pharr's [38]. Concerning the aluminum layer, the model of Loubet [40] was used to determine contact depth during indentation, given the presence of pile-up surrounding residual indents. Hardness ($H$) was obtained using equation Equation (2) and was averaged for indentation depths more than 50nm and less than 40% of the corresponding film thickness, which is a common "rule of thumb".

$$E' = \frac{S}{2\beta}\sqrt{\frac{\pi}{A_c}} \tag{1}$$

$$H = \frac{L}{A_c} \tag{2}$$

$$\frac{1-\nu^2}{E} = \frac{1}{E'} - \frac{1-{\nu_{ind}}^2}{E_{ind}} \tag{3}$$

Evolution of reduced Young's modulus is plotted as a function of the indentation depth for Si, $SiO_2$ and Al (see Figure 2). For the silicon substrate, the reduced Young's modulus is nearly constant for indentation depths between 400nm and 2000nm. But, concerning the aluminum coating and the thermal silicon oxide, analytical models were used to extract elastic properties from these experiments [40–42], in view of the effect of stiffer underlying layers. According to the methodology proposed by Mercier et al. [41], the reduced Young's modulus ($E'$(Si)) of the bottom layer (i.e. the silicon substrate) was first assessed by averaging Young's modulus values between 400 and 2000nm (see Figure 2a). Knowing the elastic properties of the silicon substrate and the thickness of the $SiO_2$ layer, the reduced Young's modulus of the intermediate layer (i.e. the $SiO_2$ layer) was extracted from the measured composite reduced Young's modulus ($E'(SiO_2)$), using Bec's model [40, 42] (see Figure 2b). Finally, the reduced Young's modulus of the aluminum coating was determined from the measured composite reduced Young's modulus ($E'$(Al)), using elastic properties and thicknesses of each underlying layers (Si and $SiO_2$) from previous experiments, injected in the extension of the Bec's model proposed by Mercier et al. [40–42] (see Figure 2c). Young's moduli were then calculated from reduced Young's moduli using Equation (3) for each material, knowing corresponding Poisson's ratios ($\nu$) given Table 1 and knowing diamond indenter properties (with $E_{ind} \approx 1000$GPa and $\nu_{ind} = 0.07$) [43]. Young's modulus and hardness values were reported in Table 1 and are consistent with the literature [43–45]. The ALD alumina coating is approximately 20 times harder than the aluminum thin film corresponding to the indentation of a a hard, brittle, elastic coating deposited on an elastic-plastic thin film.

A scratch test was performed in parallel on the multilayer specimen with a 40nm thick ALD alumina coating, using a Nanoindenter XP$^{TM}$ (MTS Instruments), to qualitatively assess the relative resistance of the materials to scratching and the adhesion of the coating to the underlying substrate. A blunted Berkovich indenter was used to perform the scratch test, oriented in a face-forward direction, in the direction of scratching. The diamond indenter scratched only one time the sample, over a length of 700µm with a maximum normal load of 40mN (corresponding to a maximum final scratch depth of 1µm), at a constant velocity of 10µm s$^{-1}$.

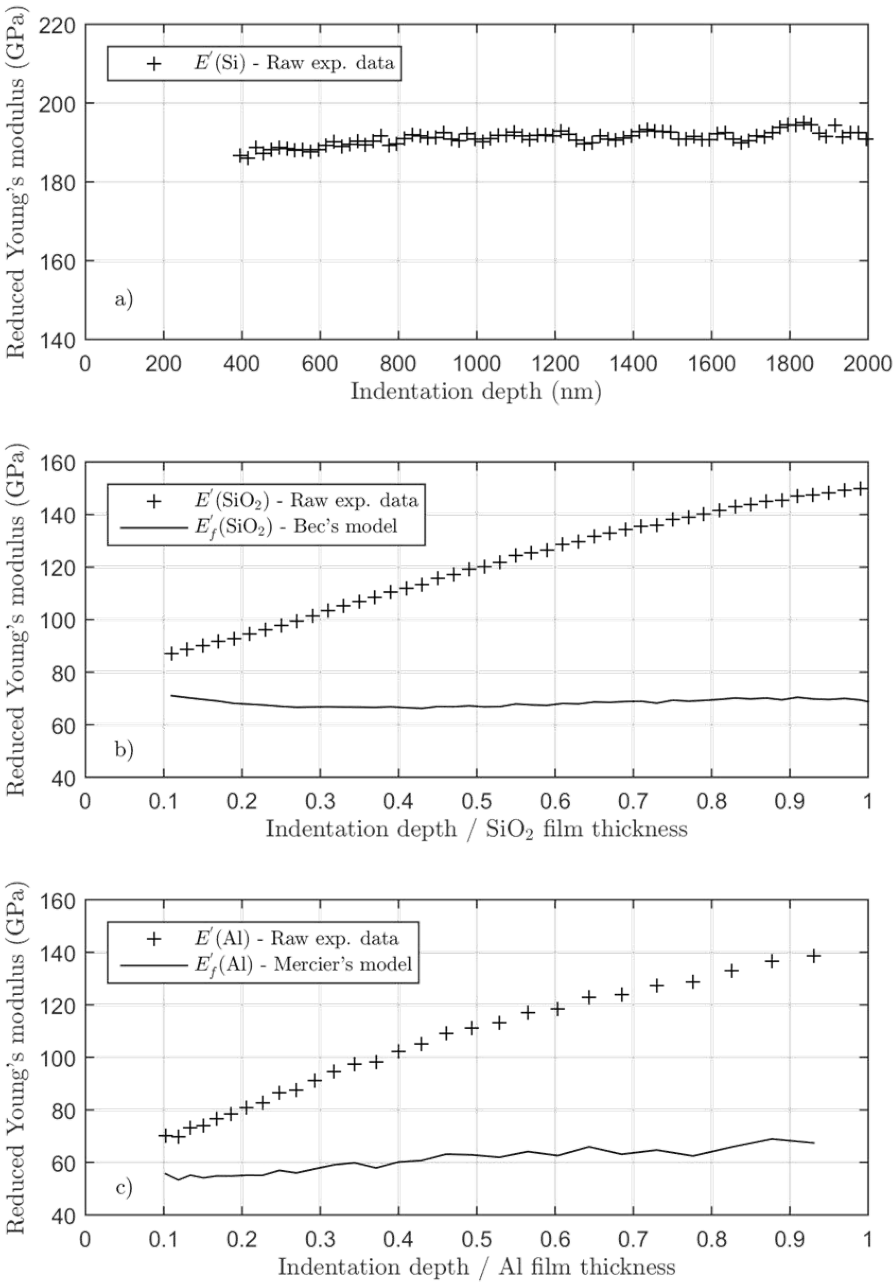


Figure 2: Evolution of the measured apparent reduced Young's modulus ($E'$) and the calculated reduced Young's modulus of the thin film ($E'_f$) in function of the indentation depth for: a) the silicon bulk, b) the thermal silicon oxide and c) the PVD aluminum thin film.

| Material | Elaboration technique | Microstructure | Thickness µm | Young's modulus ($E$) GPa | Hardness ($H$) GPa | Poisson's ratio ($\nu$) |
|---|---|---|---|---|---|---|
| Si | Czochralski process | Single crystal <100> | 725 | 173.7 ± 4.1 | 11.7 ± 0.5 | 0.28 [43] |
| $SiO_2$ | TO 1050°C | Amorphous | 0.5 | 66.7 ± 3.2 | 10.3 ± 0.4 | 0.17 [44] |
| Al | PVD | Polycrystalline | 0.54 | 53.4 ± 6.6 | 0.25 ± 0.06 | 0.34 [43] |
| $Al_2O_3$ | ALD 85°C | Amorphous | 0.01 to 0.04 | 125 ± 6 [39] | 4.83 ± 0.09 [39] | 0.24 [46] |

Table 1: A summary of morphological and mechanical properties of the different constitutive materials of the sample.

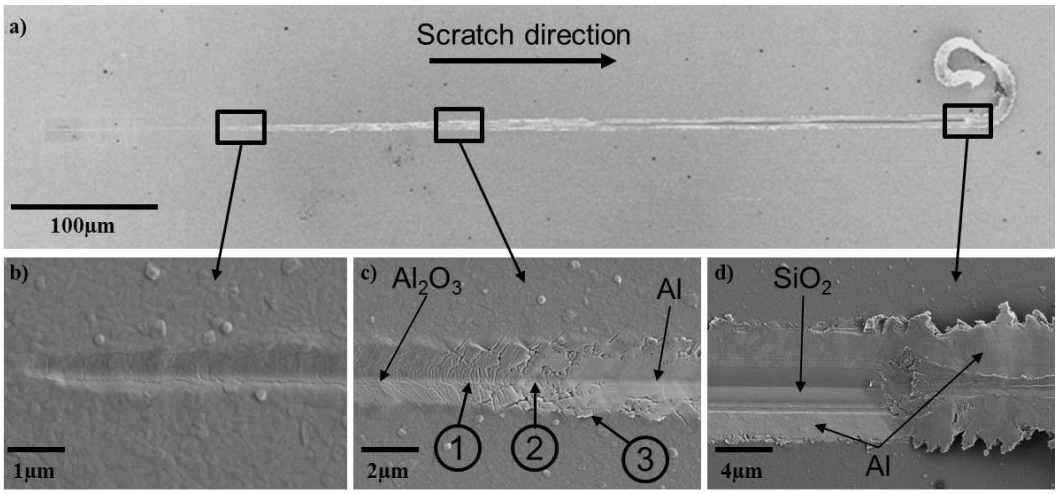


Figure 3: a) SEM observation (top view with secondary electrons) of the scratch test performed on the multilayer specimen with a 40nm thick ALD alumina coating. The different parts of the scratch experiment were magnified on the bottom part of the figure: b) start of the scratch, c) ALD alumina breakthrough and d) end of the scratch with formation of a material pile-up in front of the scratch tip.

Examination of the scratch morphology, using scanning electron microscope (SEM) micrographs illustrating the ALD alumina coating failure mechanisms (see Figure 3), revealed that failure mechanisms could be identified. Based on the failure model proposed by Holmberg [47], it is possible to distinguish three main regions of the scratch test:

- start of the scratch test with plastic deformation and minor cracks (no spallation of the coating), for normal load less than 10mN (see Figure 3b);
- major cracks and ALD alumina breakthrough (region 2), with a combination of chipping (cohesive failure - region 1) and an interfacial spalling (adhesive failure - region 3), with a normal load of 14mN (corresponding to a scratch depth of 400nm) for the coating failure (see Figure 3c) ;
- end of the scratch with penetration into the thermal silicon oxide and formation of a material pile-up in front of the scratch tip (see Figure 3d).

The characteristics of this scratch test revealed that the observed ALD alumina coating failure is mainly controlled by the plastic deformation of the aluminum underlayer. This failure mode typical for a scratch test of a hard coating on a soft substrate, was described by Bull [48] and comes from the high difference of hardness values between the ALD alumina coating (4.8GPa) and the aluminum underlayer (0.25GPa) (see Table 1). As a result, the ALD alumina coating exhibits good adhesion on PVD Al thin film and no delamination is expected to occur during spherical nanoindentation tests (with a maximum indentation depth of 400nm), presented in the following section of this paper.

# 3 Fracture through spherical indentation

## 3.1 Influence of the film thickness and the indenter tip radius

Fracture of the ALD alumina thin films was investigated by quasistatic nanoindentation with a Nanoindenter XP$^{TM}$ (MTS Instruments). Nanoindentation experiments were load-controlled and were performed using three different sphero-conical diamond tips (tip radius ($R$) of 0.45µm, 5µm and 50µm, cone angle of 90°) on a XP head, at an acquisition frequency of 10Hz and with a strain rate of 0.05s$^{-1}$. 64 measurements were carried out on 4 multilayer samples involving different thick ALD alumina coatings, respectively with thicknesses ($t$) of 10, 20, 30 and 40nm, for each indenter tip. Some typical load-displacement curves and corresponding SEM micrographs of the residual nanoindentation imprints, obtained for different ratios $R/t$, are given Figure 4.

A unique large pop-in was observed on each load displacement curve obtained for ratios $R/t \leq 500$ (see Figure 4a, 4b and 4c), and corresponding SEM observations show several radial cracks surrounding a unique circumferential crack (see Figure 4 - a'), b') and c')). For $R/t \geq 1250$, no pop-in were recorded during the indentation of the multilayer sample and the SEM micrographs presented a network of cracks, which is sometimes described in the literature as "mud-cracking" phenomenon [49]. To emphasize the difference observed in term of fracture patterns as a function of the ratio $R/t$, the SEM micrographs were processed with ImageJ software [50]. First, images were converted to binary files and an edge detection was performed in order to extract cracks networks. Fracture patterns for $R/t = 125$ (unique orthoradial crack surrounded by several radial cracks) and $R/t = 1250$ ("mud-cracking" aspect) are given respectively Figure 5a and Figure 5b. In the case of the $R/t = 1250$, radial cracks were still observed around the residual indent, but a network of entangled cracks takes the place of the unique orthoradial crack observed for lower ratio $R/t$. It seems moreover that for the ratio of $R/t = 500$, the corresponding fracture pattern is a combination of fracture patterns obtained for lower and higher ratios $R/t$. We can assume that the transition between the two processes of fracture, in the case of indentation of brittle thin film on a soft substrate is reached for a ratio $R/t$ around 500. Note that substrate plays a significant role on the pile-up formation around the indent and subsequently on the fracture of the ALD alumina at the periphery of the contact (e.g.: Figure 4-a'), when the indentation depth is close to the Al coating thickness. Nevertheless, this study focuses mainly on the first pop-in and the first orthoradial crack, which appears in the brittle layer at low indentation depths (less than 20% of aluminum layer thickness).

Some authors correlated the fracture mode to the ratios $R/t$ during spherical indentation of coating/substrate system [14, 51]. Particularly, Weppelmann E. and Swain M.V. [14] explained the formation of a first circumferential crack through a thin protective coating during spherical indentation, by carrying out a finite element analysis for ratios $R/t$ from 0.67 to 20. According to Weppelmann E. and Swain M.V, high radial tensile stresses occurred outside the contact area at the brittle coating surface, for thin films (ratios $R/t$ of 6.7 and 20). In this case, the fracture micromechanisms was dominated by a Mode I loading and cracks may already be initiated from very small preexisting flaws in the coating surface. This understanding of the crack formation was confirmed later in the literature by many authors, through numerical simulations of the indentation problem of a brittle layer on a soft substrate [26–30].

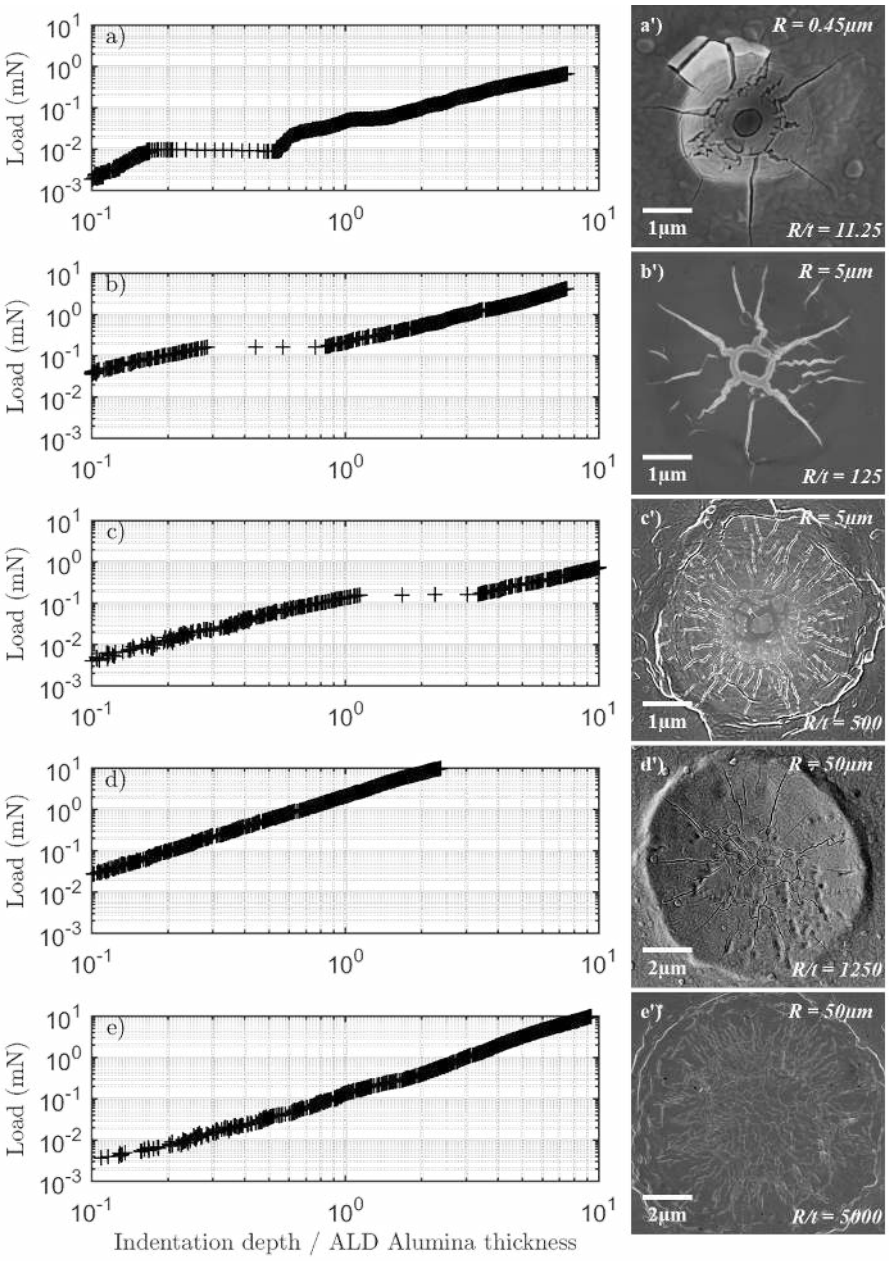


Figure 4: Typical nanoindentation load-displacement curves with corresponding SEM micrographs (top view with secondary electrons) of the residual imprint for different ratios $R/t$. Log-log plot is used to emphasize the pop-in step and to set the same scale on each graph.

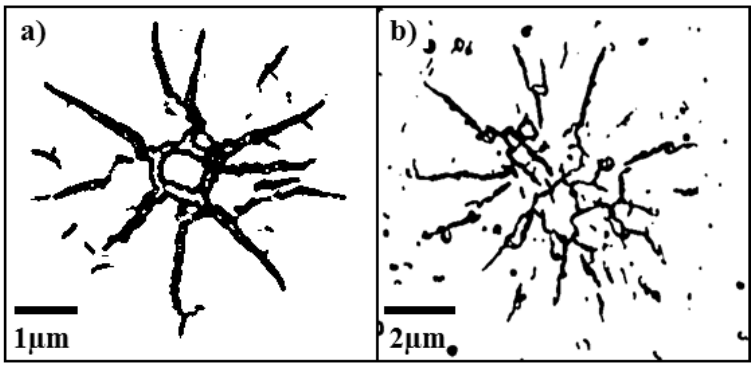


Figure 5: Fracture patterns obtained for different ratios $R/t$: a) unique orthoradial crack surrounded by several radial cracks for $R/t = 125$ and b) "mud-cracking" for $R/t = 1250$.

### 3.2 Correlation between pop-in and circumferential crack

To correlate the presence of an orthoradial crack with a plateau observed on a load-displacement curve, a specific nanoindentation program was written using the software TestWorks$^{TM}$, which was used to control nanoindentation experiments with the Nanoindenter XP$^{TM}$ (MTS Instruments). This program is based on the slope calculation of the load-displacement curve and of the displacement-time curve. A pop-in was detected as soon as both following criteria were met :

- a local slope of the load-displacement curve less than $10^{-4}\mathrm{mN\,nm^{-1}}$;
- a local slope of the displacement-time curve less than $30\mathrm{nm\,s^{-1}}$.

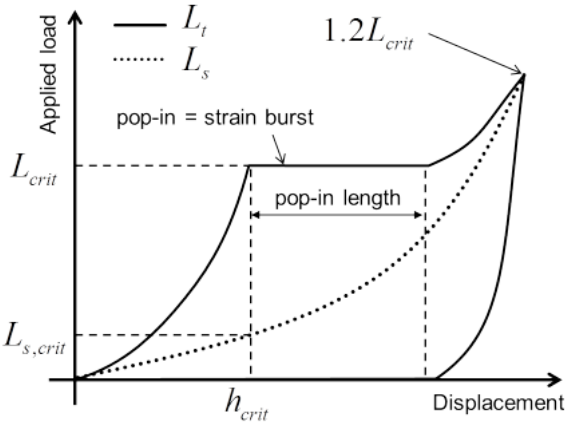


Figure 6: Schematic of the load-displacement curve programmed during nanoindentation tests to correlate pop-in event and crack formation. $L_\mathrm{t}$ is the total applied load on the sample and $L_\mathrm{s}$ is the load carried by the substrate (here the multilayer specimen without the ALD alumina coating).

These criteria correspond respectively in our experiments to a constant applied load during indentation and to a minimum pop-in length of 3nm for an acquisition frequency of 10Hz. Once the pop-in was detected at a critical load ($L_\mathrm{crit}$) for a critical indentation depth ($h_\mathrm{crit}$), the maximum load applied for the nanoindentation test was immediately set arbitrarily to $1.2L_\mathrm{crit}$ (see Figure 6), followed by final unloading. Experimental load-displacement curves recorded for ratios 11.25 and 125 and the corresponding residual imprints of indents observed by SEM, are given Figure 7. Hertzian plots of load-displacement curves before the pop-in event were plotted for each case, with the following equation:

$$L_{\text{Hertz}} = \frac{4}{3} E' \sqrt{R'} h_t^{1.5} \tag{4}$$

where $L_{\text{Hertz}}$ is the applied load for an elastic contact between a sphere and an half-space, $R'$ is the reduced radius, taken equal to the spherical tip radius, and $E'$ is the reduced Young's modulus defined either by the reduced Young's modulus of the ALD alumina coating or by the reduced Young's modulus of the aluminum layer Table 1.

Regarding Figure 7a and Figure 7c, elastic part of each load-displacement curve was correctly fitted with the Hertzian model, when the reduced Young's modulus of the aluminum layer was used in Equation (4). In parallel, an orthoradial crack was observed on each corresponding SEM micrograph (Figure 7b and Figure 7d). Based on these first observations and the literature, the sudden displacement excursion could be correlated either to nucleation/avalanche of dislocations into the aluminum thin film or to the fracture of the brittle alumina coating. However, it is not possible in our case to distinguish easily between two mechanisms on the origin of the pop-in and to determine which one occurs first or if one mechanism is causing the second one. For single crystal indentation, the first pop-in is most of the time attributed to dislocation nucleation in the metallic grain underneath the brittle oxide [9]. In this work, 5 to 10 aluminum grains were at least indented with the 0.45µm tip radius and 10 to 20 with the 5µm tip radius, which means an homogeneous plastic deformation takes place in the soft underlying polycristalline aluminum during indentation [10, 12–14, 16].

In typical indentation, only one displacement excursion and only one circumferential crack were observed (see Figure 7). But in some cases, many relatively small pop-in events (length less than 3nm) were observed on the load-displacement curve Figure 8a and a spiral-shaped crack was visible on the corresponding SEM observation Figure 8b. Such spiral morphology was already observed for Berkovich indentation on a 2.3µm NbN coating on 304L stainless steel, by Hainsworth et al. [10]. The number of segments constituting the orthoradial crack appears to be equal to the number of small displacement excursions on the load-displacement curve. Segment on the spiral-shaped crack were defined as a function of the crack curvature discontinuities. This observation suggests that loading discontinuities were related to crack formation in the alumina coating. Moreover, the deviation from the Hertzian plot at low indentation loads, before the first pop-in, suggests that plasticity can occur in the aluminum thin film before the pop-in event.

In addition, in order to verify that plastic deformation can occur prior to the fracture of the brittle alumina coating, nanoindentation was performed on the 40nm thick alumina specimen, with the 5µm tip radius, at small indentation depths. Either pure elastic deformation was taking place (loading and unloading curves were superimposed with Hertz Equation (4) and no observable residual indent or a deviation from the Hertzian plot was observed Figure 9a and a small residual imprint was visible on SEM micrographs without crack (see Figure 9b). This deviation from a pure elastic contact is either the evidence of plasticity occurring in the soft aluminum layer or the evidence of amorphous alumina layer densification. Regarding the high difference of hardness values between ALD alumina and PVD aluminum ($H(Al_2O_3) \approx 20H(Al)$), the assumption of dislocation avalanche in the aluminum film sounds highly reasonable. Finally, based on all these experimental observations, it sounds clear that the fracture of the brittle alumina coating is directly responsible of the pop-in event on the load-displacement curve.

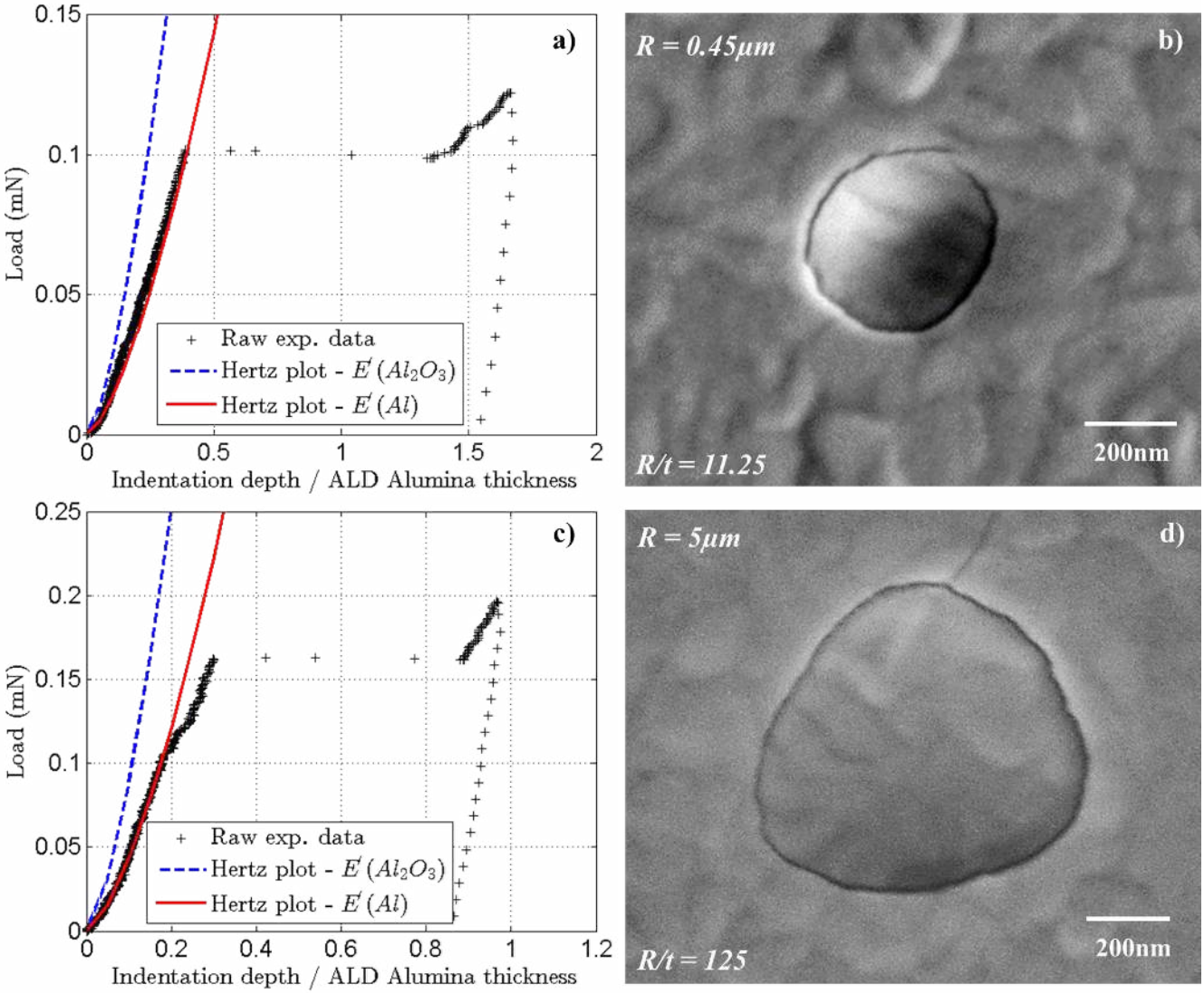


Figure 7: a) and c) are the load-displacement curves with a pop-in event and b) and d) are corresponding SEM observations (top view with secondary electrons), obtained respectively for the 0.45µm and for the 5µm tip radius, after spherical indentation on the 40nm thick alumina specimen.

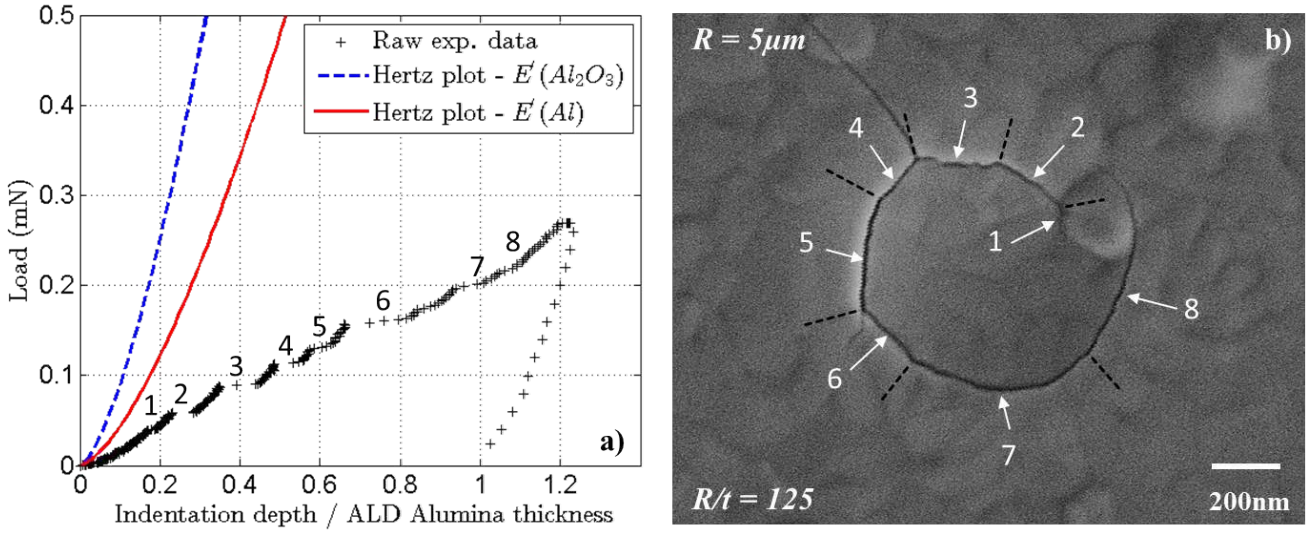


Figure 8: a) Load-displacement curve with relatively small displacement excursions, after spherical indentation on the 40nm thick alumina specimen. b) Corresponding SEM observation (top view with secondary electrons) with an orthoradial spiral-shaped crack.

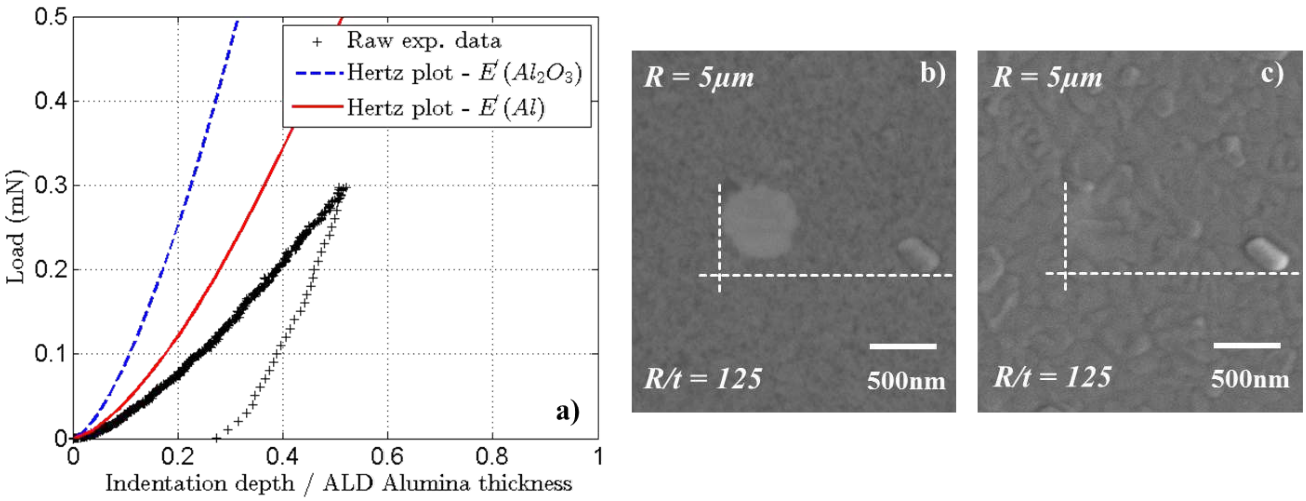


Figure 9: a) Load-displacement curve without pop-in event obtained after spherical indentation on the 40nm thick alumina specimen. b) and c) are corresponding SEM observations (top view) obtained respectively with backscattered electrons and secondary electrons.

### 3.3 Morphology of the first orthoradial crack

The morphology of the first orthoradial crack was first characterized by a cross-sectional observation prepared by focused ion beam (FIB) milling. Load-controlled nanoindentation was performed with a 0.45µm tip radius on the 40nm thick ALD alumina coating, at a maximum depth of 200nm. The SEM image of the residual indent is given in Figure 10a and the cross-section of this indent is shown in Figure 10b. The first circumferential crack is indicated on both figures with a vertical white arrow. As expected from the scratch test observations, no evidence of interfacial delamination at the ALD alumina coating / aluminum layer interface is observed. The first orthoradial crack is 10 to 20nm wide and seems to be a through thickness crack. Furthermore, no extrusion of the aluminum layer through the alumina coating was observed for such indentation depth [20].

Atomic force microscopy measurement using tapping mode was carried out on the residual indent presented Figure 7b in the previous section. Two height line profiles of this indent were plotted Figure 11b and the presence of the orthoradial crack on these profiles emphasized by step height is pointed out by black horizontal arrows. No notable pile-up compared to the surface topography, is observed on the AFM profiles given Figure 11b, for such shallow indentation test. The maximum depth of this indent is around 66nm, which corresponds reasonably to the residual indentation depth (62nm) measured on the load-displacement curve plotted Figure 7a. A maximum distance around 35nm between the specimen surface and the orthoradial crack is measured from Figure 11b (see black double arrow), whereas the pop-in is 38nm long on the load-displacement plot (see Figure 7a). This discrepancy may be due to the fact that the crack is not complete (not a perfect circle, but a spiral-shaped crack), or from the elastic recovery in the unloading process, or due to the fact that the crack formation is not initiated at the beginning of the pop-in.

It is not clear from these experiments, if the circular crack is created rapidly at once or continuously during the pop-in event. However, it is possible to determine fracture stress, using critical load and critical displacement recorded during nanoindentation experiments. Given that fracture stress is a stochastic parameter, a statistical treatment to extract average values of cracks diameter, critical load and critical displacement at which pop-in appears for different ratios $R/t$ is required.

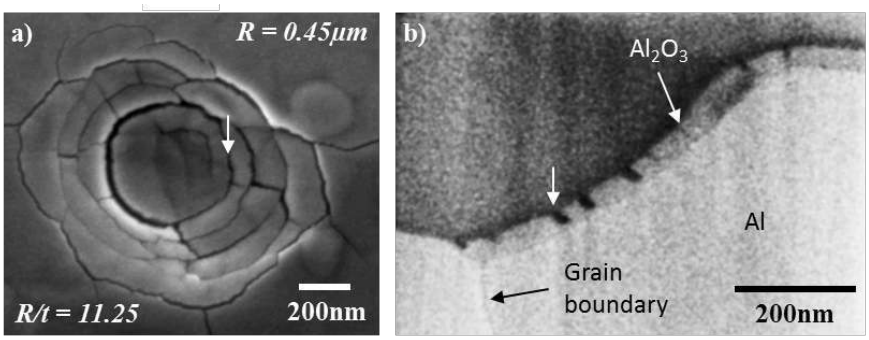


Figure 10: a) SEM micrograph (top view) of a residual imprint in the 40nm thick ALD alumina coating with FIB location (dot-dashed line) and b) a cross-sectional FIB-SEM observation of the indent with several cracks through the ALD alumina coating.

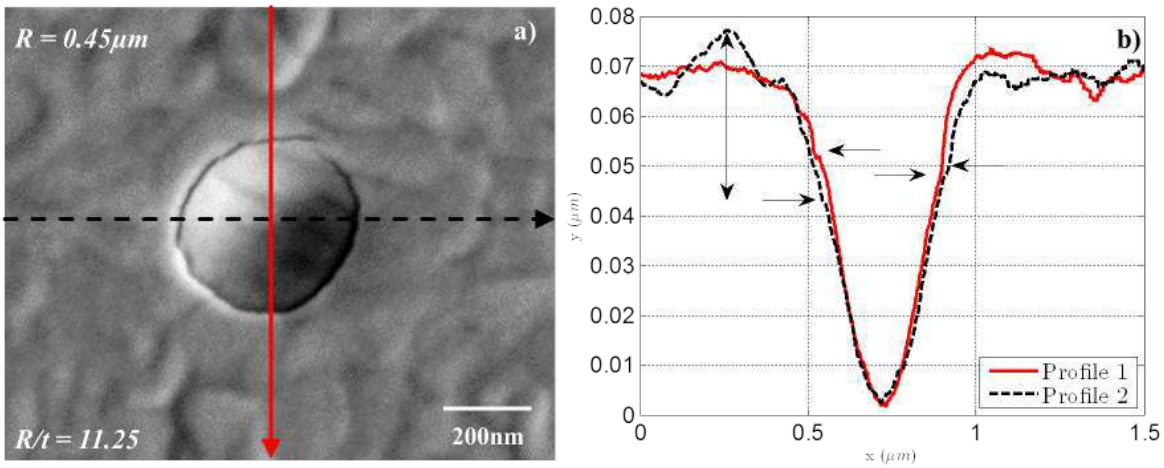


Figure 11: a) SEM observation (top view) of a residual indent in the 40nm thick ALD alumina coating with b) two height profiles obtained along the imprint topography measured by AFM.

### 3.4 Statistical analysis of the pop-in and the circumferential crack

Using nanoindentation experiments presented in the section Section 3.1, average values of the orthoradial cracks diameters, of the critical loads ($L^0_{\text{crit}}$) and of the critical displacements ($h^0_{\text{crit}}$) at which pop-in appear on load-displacement curves can be extracted for the different ratio $R/t$, but only for spherical indenters with a tip radius of respectively $R = 0.45$µm and $R = 5$µm (i.e. no "mud-cracking" observed).

From SEM observations of fracture patterns (see Figure 4 and Figure 7), it sounds that the first circumferential crack is not always a perfect circle, because of the indenter tip imperfections, the sample topography or the distribution of defects in the coating. But this first crack may consist of circular shaped crack, many circular segments of different radii or a spiral with a non-constant radius (see Figure 12). To calculate a mean diameter $\overline{D}$ for this first "circular" crack, equation Equation (5) is used with $r_i$ a measured crack radius from SEM micrographs and $n$ the total number of segments for a multi-circular segmented crack or a parameter imposed usually to 4, for a circular-shaped or a spiral-shaped crack. Uncertainty of a calculated mean diameter is set to the half of the difference between the maximum radius and the minimum radius measured for a given crack. Values of mean diameters and uncertainties for the first circumferential crack were also estimated for different ratios $R/t$ (11.25, 125, 167, 250 and 500) with at least 15 SEM observations for each situation, and were reported Table 2.

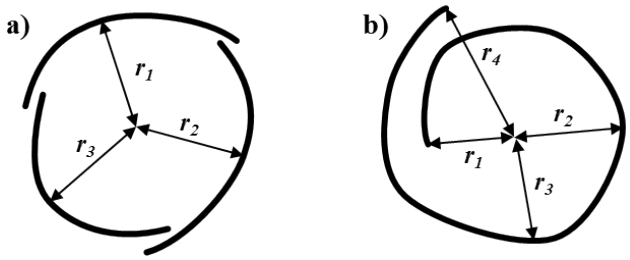


Figure 12: Schematic patterns of: a) a multi-circular segmented crack and b) a spiral-shaped crack.

$$\overline{D} = \frac{\sum_{i=1}^{n} 2r_i}{n} \tag{5}$$

A method combining the derivative ($dL/dh$) of load-displacement curve with a peak detection, was used to determine when a pop-in occurs [52]. This method is based on the same criteria used for pop-in detection implemented in the TestWorks$^{TM}$ software (see Section 3.2) (the slope of load-displacement curve tending to zero and the length of the corresponding plateau larger than 3nm). It is also possible to extract values of the critical loads ($L_{\text{crit}}$) and of the critical displacements ($h_{\text{crit}}$) (see Figure 6) for all nanoindentation tests performed for all ratios $R/t$. Based on the results of Chechenin et al. [8], a Weibull-type model was chosen for the statistic description of the breakthrough of the ALD alumina thin films. The relations (6) and (7) are the cumulative Weibull distribution functions used in our fracture analysis.

$$W\left(\frac{L_{\text{crit}}}{L^0_{\text{crit}}}\right) = 1 - \exp\left(-ln\,(2)\left(\frac{L_{\text{crit}}}{L^0_{\text{crit}}}\right)^{m_{\text{L}}}\right) \tag{6}$$

$$W\left(\frac{h_{\text{crit}}}{h^0_{\text{crit}}}\right) = 1 - \exp\left(-ln\,(2)\left(\frac{h_{\text{crit}}}{h^0_{\text{crit}}}\right)^{m_{\text{h}}}\right) \tag{7}$$

The average critical load ($L^0_{\text{crit}}$) and the average critical displacement ($h^0_{\text{crit}}$) were chosen in such way that it gives probability ($W$) of 0.5 for respectively $L_{\text{crit}}/L^0_{\text{crit}} = 1$ and $h_{\text{crit}}/h^0_{\text{crit}} = 1$. Probabilities ($W$) obtained experimentally were also plotted respectively in function of the critical load and the critical displacement (see Figure 13). Then, a least-squares fitting was done to extract the Weibull coefficients $m_{\text{h}}$ and $m_{\text{L}}$ and the different average critical parameters, which were all given in Table 2. Upon $Al_2O_3$ film thickness, no trend is observed on the critical parameters or on the Weibull coefficients evolution, for nanoindentation performed using a spherical indenter tip with radius of 0.45µm. But, with the 5µm radius spherical indenter, it seems that average values for the critical load, the critical displacement

and the orthoradial crack tends to increase with the thickness of the ALD alumina thin film. Moreover, the Weibull coefficients $m_{\mathrm{L}}$ and $m_{\mathrm{h}}$ are both between 1.5 and 2.4, which are relatively low Weibull exponents. This result indicates a high scatter of the fracture process during nanoindentation and that the ALD alumina thin films are really brittle, with a high defect size dispersion. These statistical results are coherent with experimental observations done by Chechenin et al. on the same type of amorphous alumina coatings (Weibull coefficients for the load comprised between 2 and 4) [8].

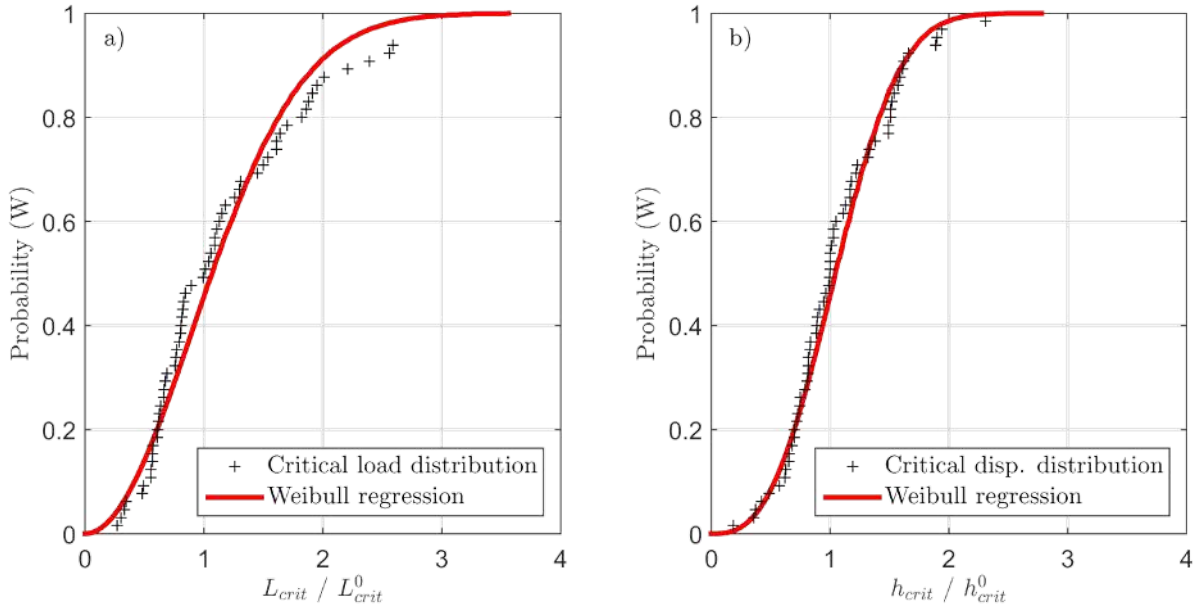


Figure 13: a) Weibull distribution of the critical load $L_{\mathrm{crit}}$ and b) Weibull distribution of the critical displacement $h_{\mathrm{crit}}$, for the ratio $R/t = 125$.

| | $R = 0.45$µm | | | | | | $R = 5$ µm | | | | | |
|---|---|---|---|---|---|---|---|---|---|---|---|---|
| ALD alumina thickness in nm | $R/t$ | $\overline{D}$ nm | $L^0_{\mathrm{crit}}$ in mN | $m_{\mathrm{L}}$ | $h^0_{\mathrm{crit}}$ in nm | $m_{\mathrm{h}}$ | $R/t$ | $\overline{D}$ nm | $L^0_{\mathrm{crit}}$ in mN | $m_{\mathrm{L}}$ | $h^0_{\mathrm{crit}}$ in nm | $m_{\mathrm{h}}$ |
| 10 | 45 | ø | 0.038 | 1.64 | 9.80 | 1.54 | 500 | $533 \pm 229$ | 0.077 | 1.90 | 10.44 | 2.05 |
| 20 | 22.5 | ø | 0.037 | 1.81 | 10.96 | 1.21 | 250 | $647 \pm 73$ | 0.089 | 2.00 | 11.48 | 1.88 |
| 30 | 15 | ø | 0.038 | 1.58 | 9.81 | 1.53 | 167 | $653 \pm 103$ | 0.091 | 2.02 | 12.24 | 1.56 |
| 40 | 11.25 | $419 \pm 35$ | 0.042 | 2.14 | 10.82 | 1.44 | 125 | $671 \pm 127$ | 0.115 | 2.26 | 18.78 | 2.37 |

Table 2: Summary of mean orthoradial crack diameters and Weibull parameters for different ratios $R/t$.

# 4 Fracture stress estimation

## 4.1 Analytical model

A brief survey of the literature shows that it is possible to approximate analytically, the fracture stress of a hard, brittle, elastic coating deposited on an elastic-plastic substrate, from indentation experiments [8, 12, 16–18, 34]. According to the literature, the elastic coating undergoes elastic deformation until brittle fracture, under indentation contact pressure and the substrate deforms plastically at relatively large loads. Hence, the deformed region of the coating is defined as an axisymmetric circular plate with a clamped edge. The clamped edge is defined as the through thickness crack into the brittle coating, which is likely located at the elastic-plastic transition in the soft substrate [12]. Assuming an approximate hemispherical plastic zone as first order and using Johnson's model, the size of the plastic zone in the substrate can be estimated by [53]:

$$c = 2\sqrt{\frac{3L_{\mathrm{s,crit}}}{2\pi\sigma_{\mathrm{e}}}} \tag{8}$$

where $c$ is the radius of the plastic zone, $L_{\mathrm{s,crit}}$ is the load carried by the substrate before the pop-in and $\sigma_{\mathrm{e}}$ the yield stress of the soft substrate. Unfortunately, this assumption is only valid when indentation experiments were performed on a brittle coating deposited on a bulk soft substrate [54]. In our case, indentation is done on a brittle alumina coating deposited on a soft aluminum thin film, which is constrained by an hard elastic substrate (thermally oxidized silicon substrate). This experiment and the evolution of the plastic zone in the aluminum thin film are schematized Figure 14. Nevertheless, it is possible to replace in our case the radius of the equivalent circular plate, by the average orthoradial crack radius. According to the membrane model (MM) of Timoshenko and Woinowsky-Krieger [55], the strength of the coating prior to its fracture ($\sigma_{\mathrm{xx,\ crit}}$) can be roughly estimated using Equation (9).

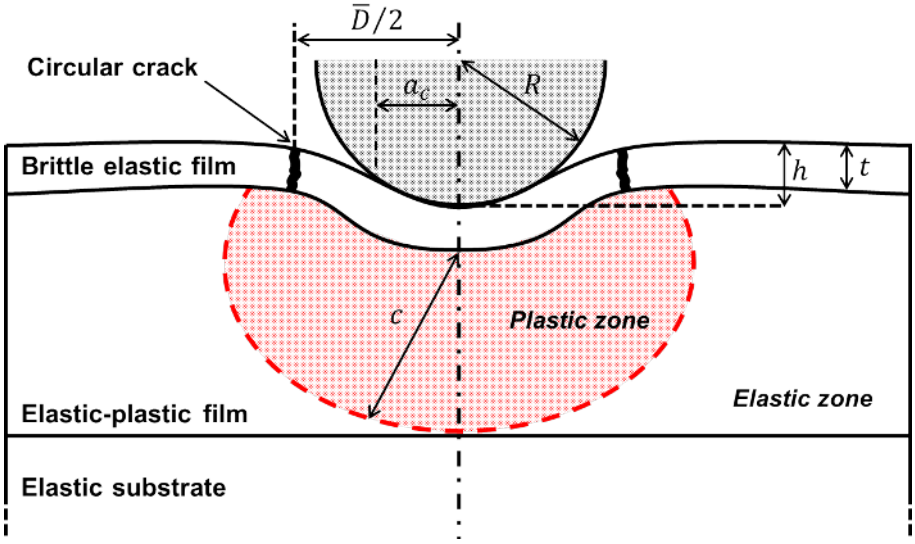


Figure 14: Schematic of spherical indentation into a brittle elastic coating on a soft elastic-plastic thin film. Here, $a_{\mathrm{c}}$ is the contact radius, $R$ is the tip radius, $c$ is the radius of plastic zone, $\overline{D}/2$ is the radius of the orthoradial crack, $h$ is the indentation depth and $t$ the ALD film thickness.

$$\sigma_{\mathrm{xx,\ crit}} = \alpha_{\mathrm{r}} E_{\mathrm{f}} \frac{w^2}{r_{\mathrm{m}}^2} + \beta_{\mathrm{r}} E_{\mathrm{f}} t \frac{w}{r_{\mathrm{m}}^2} \tag{9}$$

In Equation (9), $\alpha_{\mathrm{r}} = 0.357$ and $\beta_{\mathrm{r}} = 2.198$, are given by Timoshenko and Woinowsky-Krieger [55], $E_{\mathrm{f}}$ is the elastic modulus of the plate (here the Young's modulus of the amorphous alumina given Table 1), $t$ the thickness of the membrane (here the thickness of the alumina coating) and $w$ the deflection of the plate, which corresponds to the average critical indentation depth before rupture of the aluminum oxide ($h^0_{\mathrm{crit}}$). Stress prior to the fracture of the alumina coating was approximately estimated to be in the range of $(0.49 - 2.83)$GPa (see Table 3). This critical fracture stress decreases for thinner ALD $Al_2O_3$ film thicknesses, and increases for small spherical tip radii. This result is discussed further in this paper after numerical analysis Section 4.2.

| | $R = 0.45$µm | | | $R = 5$ µm | | |
|---|---|---|---|---|---|---|
| ALD alumina thickness in nm | $R/t$ | $\overline{D}$ nm | $\sigma_{xx,\,crit}$ in GPa | $R/t$ | $\overline{D}$ nm | $\sigma_{xx,\,crit}$ in GPa |
| 10 | 45 | ø | ø | 500 | $533 \pm 229$ | 0.49 |
| 20 | 22.5 | ø | ø | 250 | $647 \pm 73$ | 0.66 |
| 30 | 15 | ø | ø | 167 | $653 \pm 103$ | 1.01 |
| 40 | 11.25 | $419 \pm 35$ | 2.83 | 125 | $671 \pm 127$ | 1.97 |

Table 3: Summary of mean orthoradial crack diameters and fracture stresses of ALD $Al_2O_3$ using the membrane model of Timoshenko for different ratios $R/t$.

## 4.2 Numerical model

A finite element (FE) simulation of a spherical indentation of a thin hard film on a soft substrate was carried out with the commercial finite element software ABAQUS®/Standard (see Figure 15). The objective of this work was to determine the value of the maximum radial stress along the surface at the critical radial coordinate ($x_{crit}$), which is equal to half of the experimental mean orthoradial crack diameter ($\overline{D}/2$), prior to the pop-in event that occurs at the average critical depth ($h^0_{\text{crit}}$) and at the average critical load ($L^0_{\text{crit}}$), for a given geometrical configuration $R/t$. Assuming a fracture micromechanisms dominated by a Mode I loading (when $R/t \leq 500$) [14, 26–30], this radial stress ($\sigma_{xx}$), which is in traction on the surface of the top layer, should correspond to a lower bound of the fracture strength of the hard thin film.

A fully parametric FE model was created using python™[42], in order to carry out a fully automatic axisymmetric FE simulation of the indentation process. The indenter was defined as an infinite rigid body and characterized by its radius ($R = 0.45$µm or $R = 5$µm). The multilayer system was divided by default into solid elements with eight nodes and axisymmetric deformation element $CAX8R$ was adopted. The contact was defined by default frictionless for the tangential behavior and hard for the normal behavior. The external surface of the indenter was defined as the master region and the top surface of the (multilayer) sample was defined as the slave region. About the boundaries conditions, nodes were constrained along the rotation axis to prevent them from moving in the radial direction ($x$), and the nodes on the bottom surface of the sample were blocked in the radial ($x$) and vertical ($z$) directions. Indentation process was simulated by imposing a quasi-static vertical displacement to the rigid indenter along the ($z$) axis, and in each case a force ($L$) versus indentation depth ($h$) curve was extracted.

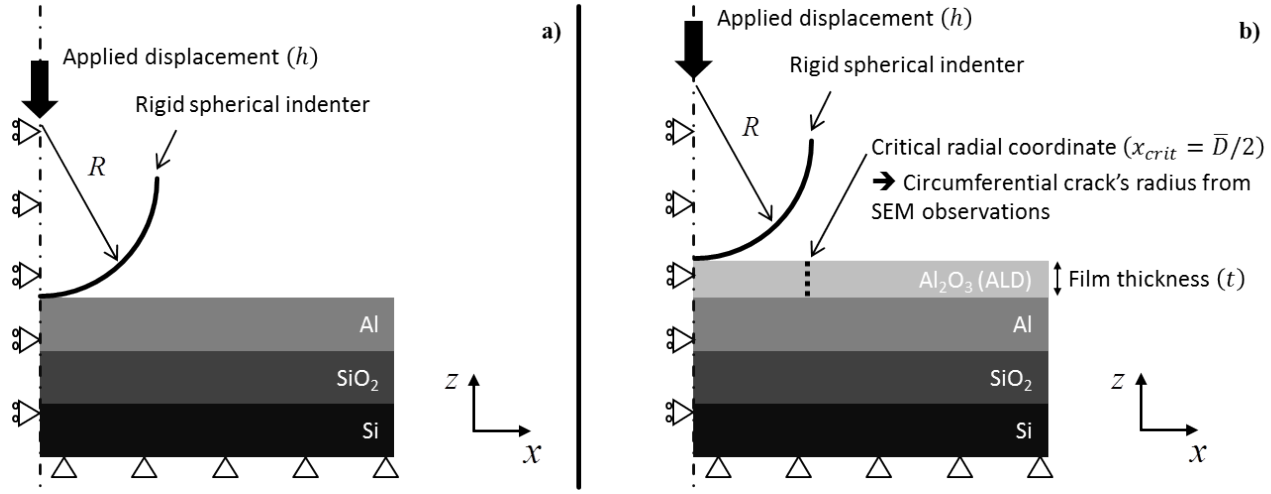


Figure 15: Schematic of the finite element modeling of spherical indentation in a multilayer sample: a) without and b) with ALD alumina coating.

Then, two multilayer systems were considered for this numerical study. Firstly, a system was modeled of an elastic-plastic film (Al) on an elastic silicon oxidized substrate to extract plastic properties of Al thin film (see Figure 15a).

Secondly, the same multilayer system with an elastic thin film ($Al_2O_3$) (see Figure 15b) to assess the fracture stress of the ALD alumina coating. All the thin films and the silicon substrate were assumed to be isotropic and were characterized by their thickness and their elastic properties (see Table 1). The thickness of the Si substrate is 5µm and the width of the two multilayer systems is 20µm. No delamination was allowed between thin films or at the film-substrate interface. The plastic behaviour of the aluminum thin film was described by the following Hollomon like power law expression as proposed by Beghini et al. [56] :

$$\sigma(\epsilon) = \begin{cases} E\epsilon & \text{if } \epsilon \leq \sigma_e/E \text{ (Hooke)} \\ \sigma_e^{1-n} E^n \epsilon^n & \text{if } \epsilon > \sigma_e/E \text{ (Hollomon)} \end{cases} \tag{10}$$

where $E_f$ is the Young's modulus of the aluminum thin film given Table 1, $\epsilon$ is the total strain (elastic + plastic). The strain-hardening coefficient $n$ and the yield stress $\sigma_e$ of the aluminum layer were positive constants to be determined from fitting. The yield stress was upper-bounded by the third of the calculated hardness value (Tabor's law - $H/3 \approx$ 83MPa) of aluminum layer given Table 1 [43].

In the first step of this numerical analysis, FE simulations of the spherical indentation on Al thin film without ALD alumina coating (with tip radii of $R = 0.45$µm and $R = 5$µm) (Figure 15a), were carried out to identify the plastic properties of aluminum ($n$ and $\sigma_e$). An optimization procedure was then employed, using the least-squares method to minimize the summed square of residuals, defined as the difference between the experimental and simulation load-displacement curves for both ratio $R/t$. The experiments have been matched by the FE model in order to achieve the best fit of experimental and simulation curves as outlined in Figure 16. The optimized work-hardening parameters of the Hollomon law are given Table 4.

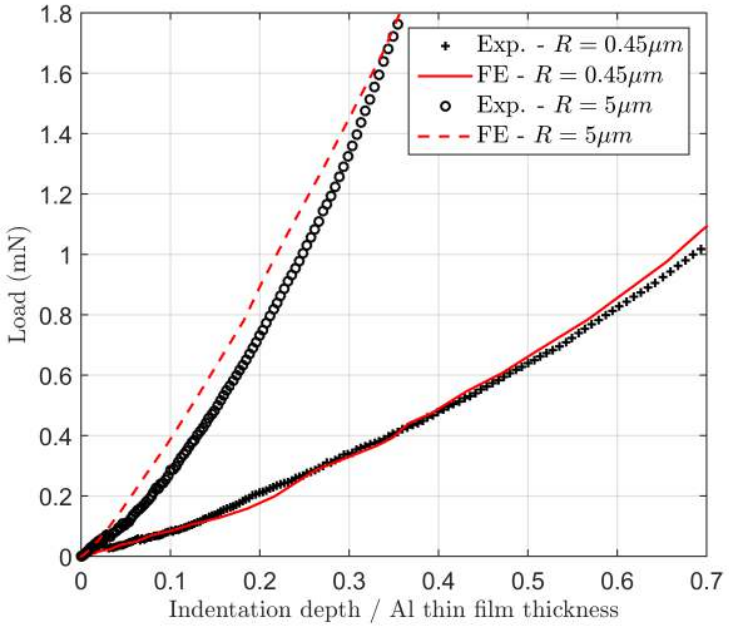


Figure 16: Comparison between experimental load-displacement curves obtained form spherical nanoindentation on Al thin film (with tip radii of $R = 0.45$µm and $R = 5$µm) and the best fitting curves based on Hollomons relationship.

| Material | $\sigma_e$ | $K$ | $n$ |
|---|---|---|---|
| PVD Al thin film | 65 MPa | 0.11 MPa | 0.08 |

Table 4: Optimized work-hardening parameters of the Hollomon law, obtained from numerical simulations of spherical indentation on Al thin film, fitted to experimental data.

In the second step of this numerical analysis, the spherical indentation on ALD alumina coating deposited on the

multilayer sample (Figure 15b), were simulated for different combinations of spherical indenter with ALD alumina coating (ratios $R/t$ = 11.25, 125, 167, 250 and 500). The evolution of the radial stress at the surface of the alumina layer was plotted as a function of the applied load normalized by the average critical load ($L^0_{\text{crit}}$) obtained from the previous statistical study of the pop-in event Figure 17. As expected, the different curves are quite close for an applied load equal to the mean critical load, and a range of surface critical stress ($\sigma_{\text{xx,crit}}$) between 0.7 and 1.5GPa was determined (see Table 5). Fracture strain ranges are calculated from the fracture stress ranges obtained analytically (Timoshenko's membrane model - MM) and numerically (FE model), using Hooke's law (Equation (10)), knowing the Young's modulus of alumina (see Table 5). An excellent agreement was observed between these ranges and values obtained by Jen et al. [57], after tensile tests of ALD alumina thin films, deposited at 155°C. Nevertheless, the observed dependence of the fracture strain with the alumina thickness is different from what Jen et al. determined experimentally. In our case, the thicker the ALD alumina coating, the higher the critical fracture strain (and thus the critical fracture stress), whereas Jen et al. measured lower critical fracture strain for thicker ALD alumina coatings. Jen et al. attributed this trend to the time between film fracture and optical measurement, the higher sensitivity of the optical probing in the current studies that allows the cracking to be visualized at lower tensile strains and surface treatments of the substrate. Here, this inverse trend is possibly due to the presence of more defects in the thicker alumina coatings and the difference between experimental conditions (spherical indentation vs tensile test). Finally, the fracture stress range determined for the ALD amorphous alumina layer is approximately 5 to 10 times less than the radial tensile stress calculated for a thermal aluminum oxide by Bahr et al. [12].

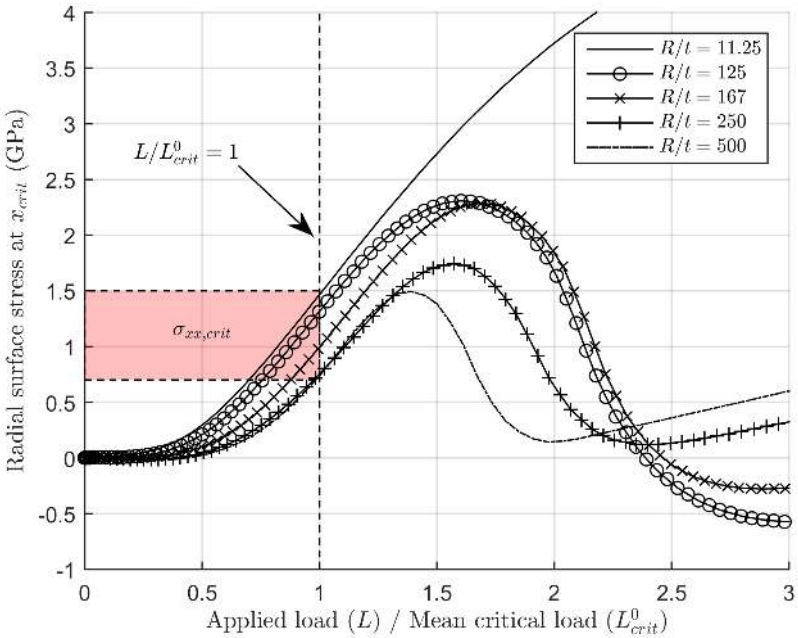


Figure 17: Evolution of the radial stress ($\sigma_{\text{xx}}$) at the surface of ALD alumina thin film as a function of the applied load, with varying ratio $R/t$.

| $Al_2O_3$ specimen | Thickness in nm | Method | Fracture stress range in GPa | Young's modulus ($E$) in GPa | Fracture strain range in % | Reference |
|---|---|---|---|---|---|---|
| ALD (85°C) | 10 to 40 | NI + MM | $0.5 - 2.8$ | $125 \pm 6$ | $0.4 - 2.2$ | This work. |
| ALD (85°C) | 10 to 40 | NI + FEM | $0.7 - 1.5$ | $125 \pm 6$ | $0.9 - 1.2$ | This work. |
| ALD (155°C) | 5 to 80 | Tensile test | - | $172 \pm 9$ [39] | $0.5 - 2.4$ | Jen et al. [57] |

Table 5: A comparison with the literature of the fracture strain ranges obtained for ALD amorphous alumina (NI: nanoindentation, MM: membrane model, FEM: finite element model).

# 5 Conclusion

In this paper, the fracture of very thin alumina coatings on a soft aluminum layer is studied. alumina films are amorphous and deposited by ALD on a multilayer specimen, which elastic-plastic properties are first characterized by Berkovich indentation. Analytical modeling is necessary to extract elastic properties of the aluminum layer and the thermal silicon oxide. A scratch test has demonstrated reasonably good adhesion of the alumina coating on the aluminum layer. Experimental observations have shown the presence of a unique orthoradial and several radial cracks in amorphous alumina and the presence of plateaus on the load vs displacement curves after spherical nanoindentation experiments, when the ratio between the spherical tip radius and the alumina thickness is equal or less than 500. Specific nanoindentation experiments with a pop-in detection is performed for ratios $R/t$ between 11.25 and 500, to correlate the formation of this unique circumferential crack with the observed displacement excursion. Nevertheless, the mechanism for creating such crack around the indentation imprint relies on the plastic deformation of the soft aluminum layer. Furthermore, a statistical analysis of the orthoradial crack's diameter and of the critical load and the critical displacement at which the pop-in appears on the load-displacement curve, is carried out to extract average values, given that fracture is a stochastic process. Distribution of the critical load and the critical displacement is assumed to follow a Weibull-type model. Low Weibull exponents is estimated, which indicates that amorphous alumina is really brittle and defects in alumina are highly scattered. From this statistical approach, an analytical study based on the membrane model proposed by Timoshenko and Woinowsky-Krieger, is applied to extract the radial stress prior to the fracture of alumina. A fracture stress range of $(0.5 - 2.8)$GPa is calculated for the ALD alumina coating for different ratios $R/t$. To validate this result, a numerical model is built and the radial stress at the expected cracking position is probed in function of the ratio $R/t$. A narrower fracture stress range of $(0.7 - 1.5)$GPa is estimated for the ALD alumina coatings, which is in agreement with analytical results and with results from the literature.

# 6 Acknowledgments

The financial support of this work under the ENIAC JEMSIP3D program was greatly appreciated.

# References

[1] M. D. Groner, F. H. Fabreguette, J. W. Elam, , S. M. George, Low-temperature al2o3 atomic layer deposition, Chemistry of Materials 16 (4) (2004) 639–645. arXiv:http://dx.doi.org/10.1021/cm0304546, doi:10.1021/cm0304546.
URL http://dx.doi.org/10.1021/cm0304546

[2] M. K. Tripp, C. Stampfer, D. C. Miller, T. Helbling, C. F. Herrmann, C. Hierold, K. Gall, S. M. George, V. M. Bright, The mechanical properties of atomic layer deposited alumina for use in micro- and nano-electromechanical systems, Sensors and Actuators A: Physical 130 - 131 (0) (2006) 419 – 429. doi:10.1016/j.sna.2006.01.029.
URL http://www.sciencedirect.com/science/article/pii/S0924424706000483

[3] C. F. Herrmann, F. W. Del Rio, S. M. George, V. M. Bright, Properties of atomic-layer-deposited $Al_2O_3$/ZnO dielectric films grown at low temperature for RF MEMS, in: M.-A. Maher, H. D. Stewart (Eds.), Micromachining and Microfabrication Process Technology X, Vol. 5715 of Society of Photo-Optical Instrumentation Engineers (SPIE) Conference Series, 2005, pp. 159–166. doi:10.1117/12.589322.

[4] T. Maindron, J.-Y. Simon, E. Viasnoff, D. Lafond, Stability of 8-hydroxyquinoline aluminum films encapsulated by a single $Al_2O_3$ barrier deposited by low temperature atomic layer deposition, Thin Solid Films 520 (23) (2012) 6876 – 6881. doi:10.1016/j.tsf.2012.07.043.
URL http://www.sciencedirect.com/science/article/pii/S0040609012008929

[5] T. Wright, T. F. Page, Nanoindentation and microindentation studies of hard carbon on 304 stainless steel, Surface and Coatings Technology 54-55 (1992) 557–562. doi:10.1016/S0257-8972(07)80082-X.
URL http://www.sciencedirect.com/science/article/pii/S025789720780082X

[6] S. K. Venkataraman, D. L. Kohlstedt, W. W. Gerberich, Continuous microindentation of passivating surfaces, Journal of Materials Research 8 (1993) 685–688. doi:10.1557/JMR.1993.0685.
URL http://journals.cambridge.org/article_S088429140001983X

[7] W. W. Gerberich, S. K. Venkataraman, H. Huang, S. E. Harvey, D. L. Kohlstedt, The injection of plasticity by millinewton contacts, Acta metallurgica et materialia 43 (4) (1995) 1569–1576.
URL http://www.sciencedirect.com/science/article/pii/095671519400351H

[8] N. G. Chechenin, J. Bøttiger, J. Krog, Nanoindentation of amorphous aluminum-oxide films .2. Critical parameters for the breakthrough and a membrane effect in thin hard films on soft substrates, Thin solid films 261 (1-2) (1995) 228–235. doi:{10.1016/0040-6090(94)06494-6}.

[9] W. W. Gerberich, J. C. Nelson, E. T. Lilleodden, P. Anderson, J. T. Wyrobek, Indentation induced dislocation nucleation: The initial yield point, Acta Materialia 44 (9) (1996) 3585–3598. doi:10.1016/1359-6454(96)00010-9.
URL http://www.sciencedirect.com/science/article/pii/1359645496000109

[10] S. V. Hainsworth, M. R. McGurk, T. Page, The effect of coating cracking on the indentation response of thin hard-coated systems, Surface and Coatings Technology 102 (1 - 2) (1998) 97 – 107. doi:10.1016/S0257-8972(97)00683-X.
URL http://www.sciencedirect.com/science/article/pii/S025789729700683X

[11] D. E. Kramer, K. B. Yoder, W. W. Gerberich, Surface constrained plasticity: oxide rupture and the yield point process, Philosophical Magazine, Part A 81 (2001) 2033–2058. doi:10.1080/01418610108216651.

[12] D. F. Bahr, C. L. Woodcock, M. Pang, K. D. Weaver, N. R. Moody, Indentation induced film fracture in hard film soft substrate systems, International Journal of Fracture 119 (2003) 339–349. doi:10.1023/A:1024979030155.
URL http://dx.doi.org/10.1023/A%3A1024979030155

[13] N. D. Madsen, S. Steffensen, H. M. Jensen, J. Bøttiger, Toughness measurement of thin films based on circumferential cracks induced at conical indentation, International Journal of Fracture 193 (2) (2015) 117–130. doi:10.1007/s10704-015-0022-5.
URL http://link.springer.com/article/10.1007/s10704-015-0022-5

[14] E. Weppelmann, M. V. Swain, Investigation of the stresses and stress intensity factors responsible for fracture of thin protective films during ultra-micro indentation tests with spherical indenters, Thin Solid Films 286 (1 - 2) (1996) 111 – 121. doi:10.1016/S0040-6090(95)08525-4.
URL http://www.sciencedirect.com/science/article/pii/S0040609095085254

[15] W. W. Gerberich, A. Strojny, K. Yoder, L.-S. Cheng, Hard protective overlayers on viscoelastic-plastic substrates, Journal of Materials Research 14 (1999) 2210–2218. doi:10.1557/JMR.1999.0297.
URL http://journals.cambridge.org/article_S0884291400050007

[16] M. Pang, D. F. Bahr, Thin-film fracture during nanoindentation of a titanium oxide film-titanium system, Journal of Materials Research 16 (2001) 2634–2643. doi:10.1557/JMR.2001.0362.

[17] K. R. Morasch, D. F. Bahr, Nanomechanical testing for fracture of oxide films, Journal of Materials Research 20 (6) (2005) 1490–1497.
URL http://journals.cambridge.org/action/displayAbstract?fromPage=online&aid=8029356&fileId=S0884291400088014

[18] K. R. Morasch, D. F. Bahr, An energy method to analyze through thickness thin film fracture during indentation, Thin Solid Films 515 (6) (2007) 3298 – 3304. doi:http://dx.doi.org/10.1016/j.tsf.2006.01.043.
URL http://www.sciencedirect.com/science/article/pii/S0040609006001507

[19] J. R. Osias, J. H. Tripp, Mechanical disruption of surface films on metals, Wear 9 (5) (1966) 388–&. doi:10.1016/0043-1648(66)90022-6.

[20] H. A. Mohamed, J. Washburn, Mechanism of solid state pressure welding, Welding Journal 54 (9) (1975) S302–S310.
URL ://WOS:A1975AN70000010

[21] P. G. Slade, Electrical Contacts: Principles and Applications / edited by Paul G. Slade, Electrical Engineering and Electronics Series, New York : Marcel Dekker, 1999.
URL http://books.google.de/books?id=EkStW7v8VPkC

[22] D. Mercier, V. Mandrillon, A. Holtz, F. Volpi, M. Verdier, Y. Bréchet, Quantitative evolution of electrical contact resistance between aluminum thin films, in: Electrical Contacts (Holm), 2012 IEEE 58th Holm Conference on, 2012, pp. 1–8. doi:10.1109/HOLM.2012.6336550.

[23] J. B. Pethica, D. Tabor, Contact of characterised metal surfaces at very low loads: Deformation and adhesion, Surface Science 89 (1 - 3) (1979) 182 – 190. doi:10.1016/0039-6028(79)90606-X.
URL http://www.sciencedirect.com/science/article/pii/003960287990606X

[24] D. D. Stauffer, R. C. Major, D. Vodnick, J. H. Thomas, J. Parker, M. Manno, C. Leighton, W. W. Gerberich, Plastic response of the native oxide on Cr and Al thin films from in situ conductive nanoindentation, Journal of Materials Research 27 (2012) 685–693. doi:10.1557/jmr.2011.432.

[25] G. E. McGuire, S. Hofmann, B. D. Sartwell, Metallurgical Coatings and Thin Films 1992, 1st Edition, Elsevier, 1992.

[26] R. M. Souza, G. G. W. Mustoe, J. J. Moore, Finite-element modeling of the stresses and fracture during the indentation of hard elastic films on elastic-plastic aluminum substrates, Thin Solid Films 355 - 356 (0) (1999) 303 – 310. doi:10.1016/S0040-6090(99)00505-2.

[27] R. M. Souza, G. G. W. Mustoe, J. J. Moore, Finite element modeling of the stresses, fracture and delamination during the indentation of hard elastic films on elasticplastic soft substrates, Thin Solid Films 392 (1) (2001) 65 – 74. doi:10.1016/S0040-6090(01)00959-2.

[28] R. M. Souza, A. Sinatora, G. G. W. Mustoe, J. J. Moore, Numerical and experimental study of the circular cracks observed at the contact edges of the indentations of coated systems with soft substrates, Wear 251 (1 - 12) (2001) 1337 – 1346. doi:10.1016/S0043-1648(01)00778-5.

[29] A. Abdul-Baqi, E. Van der Giessen, Numerical analysis of indentation-induced cracking of brittle coatings on ductile substrates, International Journal of Solids and Structures 39 (6) (2002) 1427 – 1442. doi:10.1016/S0020-7683(01)00280-3.
URL http://www.sciencedirect.com/science/article/pii/S0020768301002803

[30] K. Sriram, R. Narasimhan, S. K. Biswas, A numerical fracture analysis of indentation into thin hard films on soft substrates, Engineering Fracture Mechanics 70 (10) (2003) 1323 – 1338. doi:10.1016/S0013-7944(02)00112-1.

[31] S. K. Vanimisetti, R. Narasimhan, A numerical analysis of spherical indentation response of thin hard films on soft substrates, International Journal of Solids and Structures 43 (20) (2006) 6180–6193. doi:10.1016/j.ijsolstr.2005.05.032.
URL http://linkinghub.elsevier.com/retrieve/pii/S0020768305003136

[32] Y. Xiao, W. Shi, J. Luo, Indentation for evaluating cracking and delamination of thin coatings using finite element analysis, Vacuum 122 (2015) 17–30. doi:10.1016/j.vacuum.2015.09.003.
URL http://linkinghub.elsevier.com/retrieve/pii/S0042207X15300579

[33] M. R. McGurk, H. W. Chandler, P. C. Twigg, T. F. Page, Modelling the hardness response of coated systems: the plate bending approach, Surface and Coatings Technology 68 - 69 (0) (1994) 576 – 581. doi:10.1016/0257-8972(94)90220-8.
URL http://www.sciencedirect.com/science/article/pii/0257897294902208

[34] D. Rodriguez-Marek, D. F. Bahr, M. Pang, Mechanical measurements of passive film fracture on an austenitic stainless steel, Metallurgical and Materials Transactions A 34 (6) (2003) 1291–1296. doi:10.1007/s11661-003-0240-8.
URL http://link.springer.com/article/10.1007/s11661-003-0240-8

[35] X. Li, D. Diao, B. Bhushan, Fracture mechanisms of thin amorphous carbon films in nanoindentation, Acta Materialia 45 (11) (1997) 4453 – 4461. doi:10.1016/S1359-6454(97)00143-2.
URL http://www.sciencedirect.com/science/article/pii/S1359645497001432

[36] J. Malzbender, G. de With, Energy dissipation, fracture toughness and the indentation load - displacement curve of coated materials, Surface and Coatings Technology 135 (1) (2000) 60 – 68. doi:10.1016/S0257-8972(00)00906-3.
URL http://www.sciencedirect.com/science/article/pii/S0257897200009063

[37] P. van der Varst, G. de With, Energy based approach to the failure of brittle coatings on metallic substrates, Thin Solid Films 384 (2001) 85–89. doi:10.1016/S0040-6090(00)01801-0.

[38] W. C. Oliver, G. M. Pharr, Measurement of hardness and elastic modulus by instrumented indentation: Advances in understanding and refinements to methodology, Journal of materials research-Pittsburgh then Warrendale. 19 (1) (2004) 3–20.
URL http://journals.cambridge.org/production/action/cjoGetFulltext?fulltextid=8029500

[39] S. J. Bull, Mechanical response of atomic layer deposition alumina coatings on stiff and compliant substrates, Journal of Vacuum Science Technology A: Vacuum, Surfaces, and Films 30 (1) (2012) 01A160–01A160–8. doi:10.1116/1.3670401.

[40] S. Bec, J. L. Tonck, A.and Loubet, A simple guide to determine elastic properties of films on substrate from nanoindentation experiments, Philosophical Magazine 86 (33–35) (2006) 5347–5358.

[41] D. Mercier, V. Mandrillon, M. Verdier, Y. Bréchet, Mesure de module d'Young d'un film mince à partir de mesures expérimentales de nanoindentation réalisées sur des systèmes multicouches, Matériaux & Techniques 99 (2011) 169–178. doi:10.1051/mattech/2011029.
URL http://www.mattech-journal.org

[42] D. Mercier, NIMS toolbox, https://github.com/DavidMercier/NIMS (2015).

[43] A. C. Fischer-Cripps, Nanoindentation, 3rd Edition, Springer, 2011.
URL http://dx.doi.org/10.1007/978-1-4419-9872-9

[44] B. El-Kareh, Fundamentals of Semiconductor Processing Technology, Springer US, Boston, MA, 1995.
URL http://dx.doi.org/10.1007/978-1-4615-2209-6

[45] D. T. Read, Y.-W. Cheng, J. D. McColskey, R. R. Keller, Mechanical Behavior of Contact Aluminum Alloy, MRS Online Proceedings Library 695 (2001) null–null. doi:10.1557/PROC-695-L6.11.1.

[46] J. Thurn, R. F. Cook, Mechanical and thermal properties of physical vapour deposited alumina films Part II Elastic, plastic, fracture, and adhesive behaviour, Journal of materials science 39 (15) (2004) 4809–4819.
URL http://link.springer.com/article/10.1023/B:JMSC.0000035319.81486.62

[47] K. Holmberg, A. Laukkanen, H. Ronkainen, K. Wallin, S. Varjus, J. Koskinen, Tribological contact analysis of a rigid ball sliding on a hard coated surface Part I: Modelling stresses and strains, Surface & Coatings technology 200 (12-13) (2006) 3793–3809. doi:{10.1016/j.surfcoat.2005.03.040}.

[48] S. J. Bull, Failure mode maps in the thin film scratch adhesion test, Tribology International 30 (7) (1997) 491–498.

[49] S. Bhowmick, A. N. Kale, V. Jayaram, S. K. Biswas, Contact damage in TiN coatings on steel, Thin Solid Films 436 (2) (2003) 250–258. doi:10.1016/S0040-6090(03)00598-4.
URL http://www.sciencedirect.com/science/article/pii/S0040609003005984

[50] C. A. Schneider, W. S. Rasband, K. W. Eliceiri, NIH Image to ImageJ: 25 years of image analysis, Nature Methods 9 (7) (2012) 671–675. doi:10.1038/nmeth.2089.
URL http://www.nature.com/nmeth/journal/v9/n7/full/nmeth.2089.html

[51] C. He, Z. Xie, Z. Guo, H. Yao, Fracture-mode map of brittle coatings: theoretical development and experimental verification, Journal of the Mechanics and Physics of Solidsdoi:10.1016/j.jmps.2015.06.005.
URL http://www.sciencedirect.com/science/article/pii/S0022509615001544

[52] D. Mercier, PopIn toolbox, https://github.com/DavidMercier/PopIn (2015).

[53] D. Kramer, H. Huang, M. Kriese, J. Robach, J. Nelson, A. Wright, D. Bahr, W. W. Gerberich, Yield strength predictions from the plastic zone around nanocontacts, Acta Materialia 47 (1) (1998) 333–343. doi:10.1016/S1359-6454(98)00301-2.
URL http://www.sciencedirect.com/science/article/pii/S1359645498003012

[54] D. E. Kramer, A. A. Volinsky, N. R. Moody, W. W. Gerberich, Substrate effects on indentation plastic zone development in thin soft films, Journal of Materials Research 16 (11) (2001) 3150–3157.
URL http://journals.cambridge.org/abstract_S0884291400065158

[55] S. P. Timoshenko, S. Woinowsky-Krieger, Theory of plates and shells, 2nd Edition, Engineering societies monographs, McGraw-Hill, New York, 1987.

[56] M. Beghini, L. Bertini, V. Fontanari, Evaluation of the stress-strain curve of metallic materials by spherical indentation, International Journal of Solids and Structures 43 (7-8) (2006) 2441–2459. doi:10.1016/j.ijsolstr.2005.06.068.
URL http://linkinghub.elsevier.com/retrieve/pii/S002076830500363X

[57] S.-H. Jen, J. A. Bertrand, S. M. George, Critical tensile and compressive strains for cracking of $Al_2O_3$ films grown by atomic layer deposition, Journal of Applied Physics 109 (8) (2011) 084305. doi:http://dx.doi.org/10.1063/1.3567912.
URL http://scitation.aip.org/content/aip/journal/jap/109/8/10.1063/1.3567912